

Tuning sizes, morphologies, and magnetic properties of mono- vs. multi-core iron oxide nanoparticles through control of added water in the polyol synthesis

Gauvin Hemery^a, Anthony C. Keyes Jr.^a, Eneko Garaio^{b*}, Irati Rodrigo^{b,c}, Jose Angel Garcia^{c,d}, Fernando Plazaola^b, Elisabeth Garanger^a, Olivier Sandre^{a*}

^a LCPO, CNRS UMR 5629/ Univ. Bordeaux/ Bordeaux-INP, ENSCBP 16 avenue Pey Berland, 33607 Pessac, France

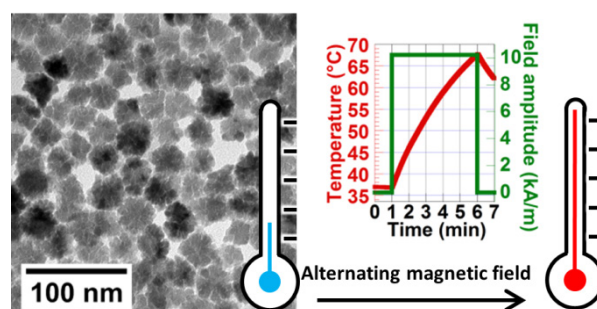
^b Elektrizitatea eta Elektronika Saila, UPV/EHU, 48940 Leioa, Spain

^c BCMaterials, Parque Tecnológico de Bizkaia, Ed. 50, 48160 Derio, Spain

^d Fisika Aplikatua II Saila, UPV/EHU, 48940 Leioa, Spain

KEYWORDS: Polyol synthesis, iron oxide, nanoparticles, magnetic hyperthermia, MRI contrast agent, nanoflowers

ABSTRACT: The polyol route is a versatile and up-scalable method to produce large batches of iron oxide nanoparticles with well-defined structure and magnetic properties. Controlling parameters such as temperature and duration of reaction, heating profile, nature of polyol solvent or of organometallic precursors were reported in previous studies of literature, but none of them described yet the crucial role of water in the forced hydrolysis pathway, whose presence is mandatory for nanoparticle production. This communication investigates the influence of the water amount and temperature at which it is injected in the reflux system for either pure polyol or mixture with a poly(hydroxy) amine. Distinct morphologies of nanoparticles were thereby obtained, from ultra-ultra-small smooth spheres down to 4 nm in diameter to large ones up to 37 nm in diameter. Nanoflowers were also synthesized, which are well-defined multi-core assemblies with narrow grain size dispersity. A diverse and large library of samples was obtained by playing on the nature of solvents and amount of water traces while keeping all the other parameters fixed. The varied morphologies lead to magnetic nanoparticles well-fitting to required applications among magnetic hyperthermia and MRI contrast agent, or both.



INTRODUCTION

Magnetic iron oxide nanoparticles (IONPs) find applications in the biomedical field as diagnostic tools and innovative therapies as they provide contrasting properties in magnetic resonance imaging (MRI) and also serve as heat mediators in magnetic fluid hyperthermia (MFH) and for triggered drug delivery.¹ As IONPs are biocompatible, they are among the best candidates over alternative magnetic nanomaterials for health applications. Various synthesis pathways have been explored for their production,² the most common being alkaline co-precipitation,³ polyol process,⁴ thermal degradation of organometallic precursors,⁵ and hydrothermal treatment⁶. The polyol process is an interesting compromise when taking into account the ease of synthesis, scalability, cost-efficiency, and control over the morphology. This process leads to nanoparticles with morphologies ranging from smooth spheres to more complex structures such as the so-called “nanoflowers”. Other strategies were reported to directly produce flower-like structures in water such as co-precipitation in presence of excess polysaccharide⁷ or in a microwave reactor.⁸ The polyol synthesis of multi-core magnetic NPs was introduced by Caruntu *et al.*⁴ In their reaction pathway, the solvent acts simultaneously as a complexing agent for

iron chloride precursors and as a high boiling point solvent, with reflux temperatures usually in the order of 220 °C. Nanoflowers are amongst the best IONPs in terms of efficiency for heating under an applied alternating magnetic field (AMF) and as negative (transverse T_2) MRI contrast agents, as previously reported.⁹ At equivalent concentrations of iron, the outstanding heating properties of these assemblies of small grains into larger raspberry-like structures were related to a frustrated super-spin glass state.¹⁰ Regarding mechanistic pathway of the synthesis, tentative descriptions of the intermediary states of reaction were proposed,¹¹ together with the role of polyol solvent in orienting the morphology.¹² Different reaction conditions were studied in literature, with control parameters such as the choice of polyol solvent,¹² temperature and pressure,¹³ reaction time and heating ramp slope,¹⁴ alkaline pH,¹⁵ and presence of adsorbed capping agents¹⁶. The main applications envisioned for nanoflowers are as nanoheaters for MFH and efficient negative (T_2) contrast agents for MRI, as ascribed to their large magnetic moment and large intrinsic magnetization M_d (magnetic mono-domain moment divided by the particle volume). The main challenge to overcome for utilizing these superior magnetic properties in biological media is to prevent

particle aggregation that can be revealed by a non-reversible magnetization curve in static magnetic field. With large magnetic moments, nanoflowers experiment strong magnetic dipolar interactions. Moreover, the coating of their surface by a residual organic layer can render them difficult to peptize as stable aqueous colloidal suspensions, especially in physiological media.

In this study, we were primarily interested in reproducing results described in the literature. However, reproducing the synthesis with published protocols proved to be a challenging task, as magnetic nanoparticles could not be obtained straightforwardly. Working in even more controlled conditions (absence of moisture, oxygen-free environment) did not help, until it was realized that traces of water were needed to perform the reaction. These observations lead to an extensive study reported hereafter, describing how the amount and way of adding water in the synthesis influence the final morphology of the NPs. A full library of water-dispersible IONPs was successfully synthesized, with tunable diameters from ~ 4 to ~ 37 nm.

MATERIALS AND METHODS

Materials

Nitric acid (HNO_3 , 70%) was from Fisher, ethyl acetate (>99.5%) was from Sigma Aldrich, acetone (technical grade), ethanol (96%), diethyl ether (100%) were from VWR, *N*-methyldiethanolamine (NMDEA, 99%), was from Acros Organics, diethylene glycol (DEG, 99%), sodium hydroxide pellets (NaOH , 98%), iron(III) nitrate nonahydrate ($\text{Fe}(\text{NO}_3)_3 \cdot 9\text{H}_2\text{O}$, >98%), and iron(II) chloride tetrahydrate ($\text{FeCl}_2 \cdot 4\text{H}_2\text{O}$, 98%) were from Alfa Aesar, iron(III) chloride hexahydrate ($\text{FeCl}_3 \cdot 6\text{H}_2\text{O}$, >97%) was from Panreac.

Synthesis of iron oxide nanoparticles

The nanoparticles were produced by modifying reaction conditions previously reported by Caruntu *et al.*:⁴ 80 mL of a mixture of DEG and NMDEA with volume ratios of either 1:0 or 1:1 v/v was added in a three-neck round bottom flask flushed with nitrogen under magnetic stirring for one hour. 1.08 g (4 mmol) of $\text{FeCl}_3 \cdot 6\text{H}_2\text{O}$ and 0.40 g (2 mmol) of $\text{FeCl}_2 \cdot 4\text{H}_2\text{O}$ were then let to dissolve overnight. In the meantime, 0.64 g (16 mmol) of NaOH powder was dissolved under magnetic stirring in 40 mL of either pure DEG or a mixture of DEG and NMDEA with 1:1 v/v ratios in a separate three-neck round bottom flask. The NaOH solution was flushed by bubbling nitrogen for one hour before mixing with the mixed iron(II,III) chloride solution. The color quickly turned from yellow to deep green. The mixture was then heated up to 220 °C (temperature ramp in around 30 min) with an electronically controlled Digi-Mantle™ heating mantle (OMCA0250, Electrothermal™) set at full power, before letting the reaction occur for a determined period of time, either with or without mechanical stirring (500 rpm). Nanoparticles were then separated over a strong permanent ferrite magnet (152×101×25.4 mm³, Calamit Magneti™, Milano-Barcelona-Paris), washed three times with 1:1 v/v mixture of ethanol and ethyl acetate, once with 10 % nitric acid, twice with acetone and twice with diethyl ether, before redispersion

in water and stirring in open air to remove the solvents. At this stage, a black monophasic dispersion of NPs was obtained. 8.6 g of iron(III) nitrate was then added to the solution as a strong oxidant by heating at 80 °C for 45 min while mechanically stirring.¹⁷ The solution then turned from clear black to clear brown-orange. The nanoparticles were flocculated by addition of 10% nitric acid before finally washing them twice with acetone and twice with diethyl ether. At this stage a deep orange-black dispersion of nanoparticles was obtained. The fluid was attracted by permanent magnets while staying in a single liquid phase, confirming that a true ferrofluid was obtained.

Sample nomenclature

Each final product is designated according to the main synthesis parameters, *i.e.* the solvent (*D* for pure DEG, *N* for DEG-NMDEA 1:1), the volume of water in μL added in 120 mL solvent (the subscript *HI* or *HU* is added to specify if water was injected to the reacting mixture at solvent reflux – hot injection – or by heating-up from room temperature), and the duration time, for example *N500_{HU}-5h* (500 μL H_2O added to 120 mL DEG-NMDEA 1:1 heated up to reflux for 5 hours) or *D5000_{HI}-20m* (5000 μL H_2O added through a septum to 120 mL of dry iron(II,III) precursors in boiling DEG, then let for 20 min before cooling).

Table 1: Batch names under varying synthesis conditions. Asterisk designates a mixture reacted under “natural mixing” (*i.e.* by diffusion and convection, but no stirring).

Batch name	Nomenclature
15ff	<i>N1000_{HU}-5h</i>
17ff	<i>D5000_{HI}-20m</i>
25ff	<i>N500_{HU}-4h</i>
30ff	<i>N1000_{HU}-5h</i>
31ff	<i>N500_{HU}-1h</i>
32ff	<i>N500_{HU}-5h</i>
34ff	<i>N100_{HU}-5h*</i>
35ff	<i>N100_{HU}-5h</i>
36ff	<i>N100_{HU}-5h</i>

Transmission Electron Microscopy was performed on a Hitachi™ H7650 microscope with an acceleration voltage of 80 kV. TEM images were acquired with an ORIUS™ SC1000 large format (11 MPx) Camera. Samples were prepared by nebulizing NP dispersions at concentrations of 1 g·L⁻¹ on Formvar™ carbon coated 200 mesh copper grids from Agar Scientific™ and leaving them to dry at room temperature. NP size distributions were obtained by measuring more than 100 NPs with the ImageJ freeware (<https://imagej.nih.gov/ij/>). Size-histograms were fitted to a log-normal distribution law $P(d)$ of optimized values of median diameter α and non-dimensioned width β :

$$P(d) = \frac{1}{d \cdot \beta \sqrt{2\pi}} \cdot \exp\left(-\frac{(\ln(d) - \ln(\alpha))^2}{2\beta^2}\right)$$

In addition, the mean sizes $d_o = \langle d \rangle$ (number-averages) and standard deviations $\sigma = \langle (d - \langle d \rangle)^2 \rangle^{1/2}$ were calculated using the classical Gaussian statistics formulas.

Dynamic Light Scattering and Zetametry: A Nanosizer™ Nano ZS90 from Malvern™, UK, was used to measure ζ potentials, Z-average hydrodynamic diameters (D_h), and polydispersity indexes (PDI). 2nd order Cumulant fit was used for DLS (the PDI being defined as the ratio of the 2nd order coefficient to the square of the 1st order one in the series¹⁸), and Smoluchowski equation for zetametry.

Relaxometry: Samples were prepared at concentrations of 6 mM_{Fe}. NMR tubes (7.5 mm outer diameter) were filled with 1 mL of each sample, and inserted in a Bruker™ mq60 relaxometer equipped with a 60 MHz / 1.41 Tesla magnet. The samples were left to thermalize to 37 °C using a Julabo™ f25 ED circulation bath. Following recommended protocols in proton relaxometry,¹⁹ longitudinal T_1 relaxation times were measured using an inversion-recovery sequence of first duration of $\sim 0.1 \times T_1$ and final duration of $\sim 3 \times T_1$ with a recycling delay (RD) of $\sim 5 \times T_1$ between two of the 10 acquisition points, 4 scans and an automatic RF receiver gain. Transverse T_2 relaxation times were measured using Car-Purcell-Meiboom-Gill (CPMG) sequence, with delay time τ of 0.04 ms between the 90° rotation to transverse plane and the 180° focusing pulse, a duration time of $3 \times T_2$, RD of $5 \times T_2$, and automatic receiver gain. The number of acquisition points was set by dividing the duration time by the delay time τ .

Magnetic hyperthermia: NPs were dispersed at concentrations of 3 g·L⁻¹ in diluted HNO₃ (at pH~2) to preserve their colloidal stability. The samples were placed in 500 μ L plastic cuvettes, which caps were pierced with a needle to introduce a fiber optics temperature probe of 420 μ m outer diameter (medical range OTG-M420 fiber, Opsens™, Québec, QC, Canada) and measure temperature profiles *versus* time. Samples were thermalized at 37 °C using a glass-water jacket connected to a temperature bath until reaching equilibrium. The heat generation by magnetic NPs was triggered using an induction coil (4-turn of 3.5 mm diameter hollow – 0.4 mm wall – copper tubing, 55 mm outer diameter, 48 mm inner diameter, 34.5 mm height) fed by a Minimax Junior™ iTS 3.5 kW generator (Seit Elettronica™, Italy) applying an alternating magnetic field (AMF) at maximum amplitude H_{app} of 10.2 kA·m⁻¹ and at a frequency f of 755 kHz as determined by finite element modelling.²⁰ The amplitude and frequency of the magnetic field were corroborated by measuring the electromotive force in a scout coil (turn of 17.5 mm diameter) and an oscilloscope (Agilent™ 54641 A). The AMF was applied for 5 min while recording the elevation of temperature and measuring its slope at early times (within first 5 s).

Static (DC) magnetization curves of the NP aqueous dispersions were obtained on a 1.8 T homemade vibrating sample magnetometer (VSM, SGlker – UPV/EHU). The magnetic field was measured by a gaussmeter whereas the signal was conditioned by a Stanford™ SR810DSP lock-in amplifier controlled by a PC under a LabVIEW™ program.

Zero field cooling – field cooling (ZFC-FC) experiments were conducted on a SQUID magnetometer (MPMS™ 7T from Quantum Design™, San Diego, CA, USA). This magnetometer was previously calibrated by Y₃Fe₅O₁₂ garnet 1 mm diameter sphere (standard reference materials 2853) and reset after each measurement. Estimates of the blocking temperature and of the magnetic anisotropy were made according to a previously published protocol.²¹

Iron titration in NP suspensions: Iron molarity [Fe] was given by a disruptive photometric assay, using the characteristic absorption peak at 350 nm of [Fe(Cl)₆]₃⁻ complex when an aliquot of the suspension was dissolved in concentrated hydrochloric acid (HCl 5 M), according to previous calibration law $OD_{350nm, 2mm} = 0.5043 \times [Fe]_{mM} + 0.0172$. Then [Fe] was converted into iron oxide weight assuming pure γ -Fe₂O₃ composition (~ 80 g·mol⁻¹).

Small angle neutron scattering (SANS) curves were acquired on the PACE spectrometer of the LLB-CEA Saclay.

RESULTS AND DISCUSSIONS

This study of water effect originates from an unexpected observation made while reproducing the synthesis of iron oxide NPs first described by Caruntu *et al.*⁴ After dissolving separately iron(II,III) chlorides and sodium hydroxide in polyols in open air, NPs were produced after mixing the two solutions and elevating temperature. But in these conditions, it was noticed that the starting solution of iron chlorides slowly changed of color from brownish to yellow, as iron(II) salt was slowly oxidized into iron(III). In another experiment, the solvents were degassed beforehand with anhydrous nitrogen flow before dissolving the precursors and kept well-isolated from the open air to counter this oxidation effect. The color of the iron chlorides solution remained brownish through time, but no NPs were produced upon mixing with the sodium hydroxide solution and elevating temperature. Therefore it was postulated that in the first experiment, water traces were incorporated in the highly hygroscopic polyol solvent by agitating it in open-air, and that this water content in the reaction mixture before heating is a key parameter to produce magnetic NPs. This observation led to an extensive study of the role of water in the synthesis of iron oxide nanoparticles in a mixture of a polyol and a poly(hydroxy) amine (*viz.* DEG, NMDEA). Different batches of NPs were produced by varying reaction parameters (*e.g.* duration, solvent system, amount and time of injection of water traces, *i.e.* hot injection *vs.* heating-up).

As the two major biomedical applications of IONPs are for magnetic fluid hyperthermia (MFH) and as MRI contrast agents, we dedicated our efforts to provide selected NPs suitable for these two applications. Large (several tens of nm) NPs were produced for MFH, while ultra-ultra-small superparamagnetic iron oxide (UUSPIO) NPs of few nm only were synthesized for applications as positive MRI contrast agents with T_1 -weighted sequences.²²⁻²⁵ The main reaction parameter to select morphology (and therefore magnetic properties) was solvent composition. A mixture of DEG and NMDEA (1:1 volume ratio) was used to yield large NPs, while ultra-ultra-small NPs were

produced in pure DEG. In both cases, the same quantity and stoichiometric ratio of iron(II,III) chlorides and hydroxides were used (2:1:8 $\text{Fe}^{3+}:\text{Fe}^{2+}:\text{OH}$ ratio, i.e. one hydroxide anion per chloride).

Reactants were heated from room temperature to reflux (approximately 30 min to reach 220 °C) to obtain NPs. Traces of water were injected to the mixture either at room temperature (*heating-up*) or at reflux (*hot injection*), while solvents were freshly ordered and preserved from moisture. In the case of the DEG/NMDEA solvent system, traces of water were injected in different amounts from 100 μL to 2 mL in 120 mL of solvent, representing between 0.083 % and 1.67 % (v/v). Using lower amounts of water did not allow producing NPs, while using larger quantities of water lead to ill-defined NPs. The best control (meaning size-distribution and homogeneous morphology) was achieved when mixing a determined amount of water in the solvent system with the precursors before heating up, as supposedly ascribed to more homogeneous composition of the starting mixture.

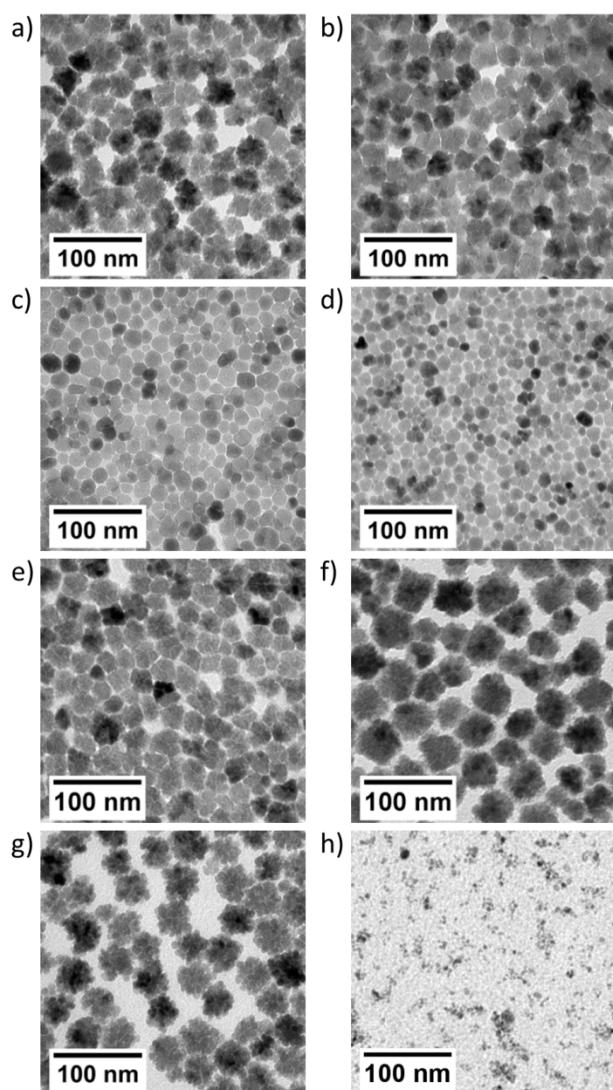


Figure 1. TEM micrographs of $\gamma\text{-Fe}_2\text{O}_3$ NPs of mono- or multi-core morphology and their measured outer diameters: a) 36ff (32.3 ± 5.0 nm), b) 35ff (29.1 ± 4.4 nm), c) 34ff (18.5 ± 3.2 nm), d)

32ff (14.5 ± 3.4 nm), e) 31ff (27.5 ± 4.2 nm), f) 30ff (46.9 ± 8.5 nm), g) 15ff (36.9 ± 4.8 nm), and h) 17ff (4.3 ± 1.1 nm).

Surprisingly, using anhydrous iron(III) chloride instead of the hexahydrate compound did not allow producing magnetic NPs, even when adding traces of water before heating. This evidences the large influence of water on the reaction, and the importance of the addition order of the chemical compounds in the outcome of reaction. In the polyol/poly(hydroxyl) amine synthesis, the solvents act simultaneously as multivalent chelators for iron(II,III) centers, as well as a high boiling temperature medium to achieve control over the nucleation and growth of NPs. The chloride counter-ions of the iron(II,III) salts can be exchanged by complexing solvent molecules and then by hydroxide ions when adding NaOH. It was described by Caruntu *et al.* that the actual precursors of inorganic polymerization are the iron(II,III) hydroxides in which the metallic centers are also chelated by DEG." Therefore the polyol route is also referred to in literature as a "forced hydrolysis" mechanism. This salt metathesis can be observed by eye when mixing the reactants from the color changes of the organometallic solutions turning into a black colloidal suspension of magnetite (Fe_3O_4) NPs.

Studying the medium of synthesis by NMR helped understanding the mechanism of reaction (Figure S2). It is observed that controlled water addition shifts the broad peak attributed to the labile protons of hydroxyls in DEG and NMDEA. Apart from further shift of this labile proton peak ascribed to pH variation occurring during synthesis (hydroxyls being converted into oxide), NMR spectrum does not show evidence of polyol molecules degradation.

It is worth noting that the IONPs are in most cases still covered by a layer of chelating solvents even after purification steps using a mixture of ethanol and ethylacetate.¹⁴ This affects the colloidal stability of the samples, and their ability to be oxidized. During the oxidation step, the sample color is expected to turn from black to brown as IONPs are oxidized from magnetite to maghemite. In some cases, especially for nanoflowers, the solution color remained black. This protective layer of DEG and NMDEA at the surface of the IONPs was evidenced by Zeta Potential measurement of the IONPs versus pH (Figures S1). The isoelectric point (IEP) of maghemite is around pH=7, while the IEP of the IONPs still covered by a layer of solvents is shifted to about pH=9, which is consistent with the expected pKa value of the amine moiety in NMDEA. Washing the IONPs by a precipitation-redispersion process in alkaline water medium revealed to be an efficient mean to remove the last traces of chelated solvents.

In the case of the pure DEG solvent, amounts of water as large as 5 mL, representing 4.2 % of solvent volume were injected at reflux temperature with a syringe needle through a septum (*hot injection*), generating smaller NPs, with diameters typically in the order of 3-5 nm. The fast introduction of water at high temperature immediately generated a sudden nuclei burst, with a solution turning from deep green to black. This hot injection method leads to "ultra-ultra-small" NPs as there is a limited quantity of

precursors in solution available for crystal growth. The time-scale of reaction was usually much shorter than when synthesizing larger NPs in DEG/NMDEA. Typically, reactions were completed after 15-20 min. When letting an aliquot of the reaction mixture at rest over a strong permanent magnet, the supernatant became uncolored, evidencing the total conversion of the colored iron(II,III) organometallic precursors into colloidal magnetite phase.

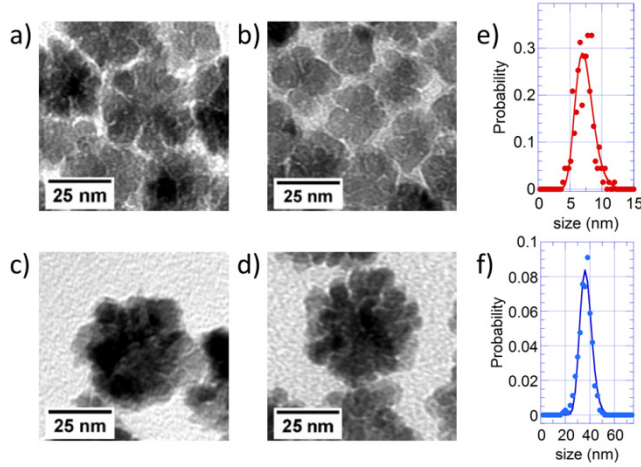


Figure 2. TEM micrographs of $\gamma\text{-Fe}_2\text{O}_3$ nanoflowers: a) 36ff, b) 35ff, c) 30ff, and d) 15ff. Distribution of grain size 7.4 ± 1.4 nm (e) and outer diameter 36.9 ± 4.8 nm (f) for the 15ff batch as measured from TEM micrographs and log-normal fits.

The final products of different batches differed greatly in sizes and in shapes. Smooth spheres and more complex structures previously reported as “nanoflowers” were obtained this way. TEM images enabled measuring both the overall diameters and the individual grain sizes for such multi-core NPs. These estimates can be compared to other available techniques for particle sizing, *e.g.* from the width of X-ray diffraction peaks, the fit of magnetization curve by the Langevin function, or of SANS curve by a polydisperse sphere form factor, the latter two methods being used here (Figures S3 and S4). Smooth spheres were produced with adjustable sizes from ~ 4 nm to ~ 20 nm, while nanoflowers were obtained with sizes from ~ 27 to ~ 37 nm (Figure 1). The size-histograms could be well-fitted using a log-normal distribution law of parameters α and β (Figure 2). In order to express diameters as $d_0 \pm \sigma$, the mean values d_0 along with standard deviations σ were calculated according to following formulas:

$$d_0 = \langle d \rangle = \alpha e^{\beta^2/2} \text{ and } \sigma^2 = \langle (d - d_0)^2 \rangle = d_0^2 (e^{\beta^2} - 1)$$

Size distributions characterized by β parameters below 0.2 were considered sufficiently narrow and suitable for further characterization. The condition $N_{100\text{HU}}5\text{h}$, under mechanical stirring, proved to be both optimal and robust for reproducible nanoflower synthesis, TEM images of 35ff and 36ff batches being comparable, as seen on Figure 2. However, identical conditions but without stirring led to smooth spherical iron oxide NPs instead (34ff), of narrow size-distribution 18.5 ± 3.2 nm by TEM analysis, or 18.8 ± 6.5 nm by fitting the DC magnetization curve (Figure S4).

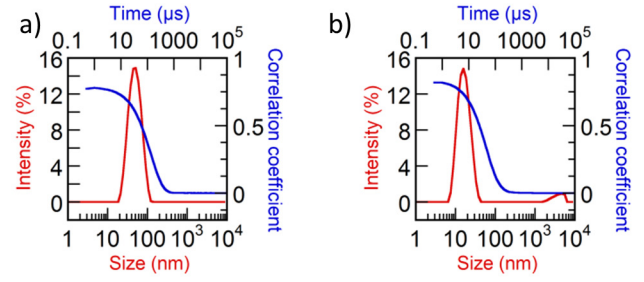


Figure 3. DLS correlograms and intensity-averaged distribution of diameters. The 2nd order cumulant fit leads to the Z-average hydrodynamic diameter and polydispersity index (PDI): $D_h = 36$ nm (PDI=0.13) for 35ff nanoflowers (a); $D_h = 16$ nm (PDI=0.21) for 20ff UUSPIO smooth spheres (b).

The dispersion state of the NP batches in a weakly acidic (pH \sim 2) aqueous medium was probed by dynamic light scattering (DLS): The fit of correlograms by the 2nd order cumulant method (Figure 3) provides the Z-average hydrodynamic diameter (D_h) and polydispersity index (PDI). Typical values of Z-average diameters were in the order of 30 nm, ranging from 16 to 55 nm when considering all synthesized batches (Figure S5). Hydrodynamic sizes and size dispersity by DLS are always larger than TEM diameters but represent the actual dispersion state of the NPs.

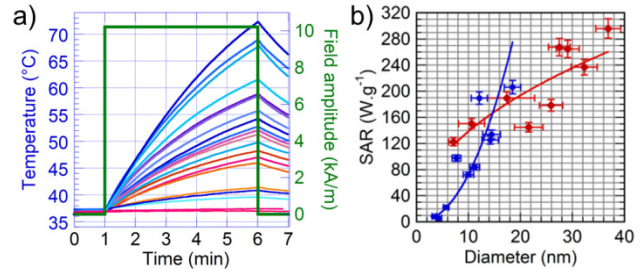


Figure 4. Temperature profiles vs. time of different samples under application of AMF at $H_{\text{app}} = 10.2 \text{ kA}\cdot\text{m}^{-1}$ and $f = 755 \text{ kHz}$ (a). Deduced SAR versus mean TEM diameter of the NPs for nanospheres (blue) and nanoflowers (red) b). Solid lines are power law fits of exponents respectively 2.2 and 0.48.

The efficiency of the different NP batches for magnetic hyperthermia was evaluated by applying an AMF for 5 min and recording the temperature rise of the samples, with iron oxide concentrations set to $3 \text{ g}\cdot\text{L}^{-1}$ in order to compare the results. While no significant heating under AMF was obtained for a few samples like the smallest size 17ff, temperature rise from 37°C to 70°C was recorded for the best sample (Figure 4). Therapeutic hyperthermia requires that injected NPs heat up the cancerous tissues at $43\text{--}44^\circ\text{C}$ to deposit a “thermal dose”. This temperature can be potentially reached by using the best heating samples after few minutes, even at a concentration lower than in this study ($3 \text{ g}\cdot\text{L}^{-1}$), given that their heating properties are preserved in physiological intracellular conditions.²⁶ The heating properties of the samples were quantified using the specific absorption rate determined experimentally using the commonly used formula:

$$\text{SAR} = (\Delta T / \Delta t)_{t \rightarrow 0} C_P / m$$

where $(\Delta T/\Delta t)_{t \rightarrow 0}$ is the temperature raise slope at early times of AMF application (first 5 s) to simulate adiabatic conditions,²⁷ m is the mass of nanoparticles in 1 mL of suspension and C_p is approximated by the specific heat of pure water. Here the SAR was used instead of the intrinsic loss power (ILP)²⁸ to evaluate the heating properties, as the SAR variation with field intensity can deviate from a quadratic law. The plot of SAR at given field amplitude ($H_{app}=10.2 \text{ kA}\cdot\text{m}^{-1}$) and frequency ($f=755 \text{ kHz}$) vs. diameter measured by TEM on **Figure 4 (b)** clearly evidences a correlation between the SAR and the TEM outer diameter of the NPs, experimentally following a quadratic law for nanospheres, and a lower exponent (nearly square-root) for nanoflowers, in qualitative agreement with the most advanced models on the optimal size of magnetic NPs for MFH at given values of their other physical properties (specific magnetization and magnetic anisotropy).²⁹ This study evidences that nanoflowers and the largest spheres find applications as magnetic nanoheaters, while smaller NPs do not generate sufficiently heat, and will be mostly useful as positive (T_1 -weighted) MRI contrast agents. Intermediate diameters in the range of 10–20 nm corresponding to large smooth spheres can be used both for MFH and as negative (T_2 -weighted) MRI contrast agents, as evidenced later in this article.

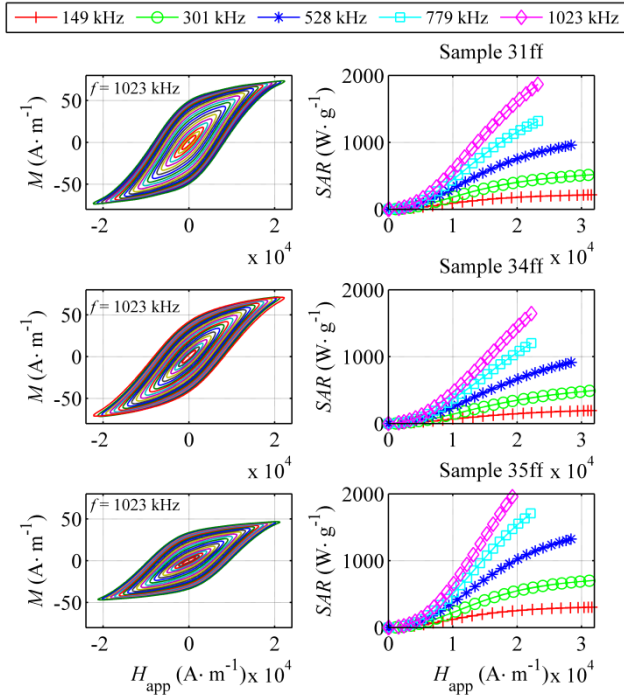


Figure 5. AC hysteresis loops of samples 31ff, 34ff and 35ff at 1023 kHz fixed frequency (left). SAR of samples 31ff, 34ff and 35ff versus field amplitude at different frequencies (right).

An in-depth characterization of magnetic heating properties was carried out on selected NP samples with interesting morphologies as evidenced by TEM, having shown satisfying SARs at $H_{app}=10.2 \text{ kA}\cdot\text{m}^{-1}$ and $f=755 \text{ kHz}$: Large smooth spheres (34ff) and nanoflowers of different grain size and increasing outer diameters (31ff<35ff<15ff). These samples were further examined with an in-house developed pick-up coil set-up allowing SAR measurement on a

broad range of AMF frequencies and amplitudes.³⁰ AC magnetization curves of NPs are plotted on **Figure 5 (left)** versus amplitude H_{app} up to $21 \text{ kA}\cdot\text{m}^{-1}$ at fixed frequency ($f=1030 \text{ kHz}$). Similar curves at other frequencies are provided in Supporting Information (**Figures S6, S7, S8 and S9**). Such hysteresis loops reflect that magnetic moments of NPs under AMF excitation oscillate with a phase lag relatively to the magnetic field, which converts part of the radiofrequency magnetic energy into heat, dissipated in the surrounding aqueous medium. Larger hysteresis loops areas are obtained at higher amplitudes and higher frequencies, while stronger magnetic anisotropy of the materials tends to change the shapes of the curves from sigmoidal to more square-like shapes: Carrey *et al.* proposed to interpret such dynamic hysteresis by a two-level Stoner-Wohlfarth model instead of the classical linear theory of Néel and Brown relaxations of the moments.^{29, 31, 32} The larger the surface of the hysteresis loop, the larger the energy dissipated by the NPs per AMF cycle. It is possible to compare these AC magnetization curves to the calorimetric experiments by multiplying by frequency the surface of a hysteresis loop and dividing by iron oxide concentration to get the SAR, and plotting the obtained value as a function of frequency and amplitude, as shown in **Figure 5 (right)**. It is evidenced that SAR values as high as $2000 \text{ W}\cdot\text{g}^{-1}$ can be obtained with a frequency of 1023 kHz and amplitude of $20 \text{ kA}\cdot\text{m}^{-1}$, although out-passing by a factor 4 the upper limit of $5 \times 10^9 \text{ A}\cdot\text{m}^{-1}\cdot\text{s}^{-1}$ of the $f \times H_{app}$ product recommended for human treatment by MFH.³³

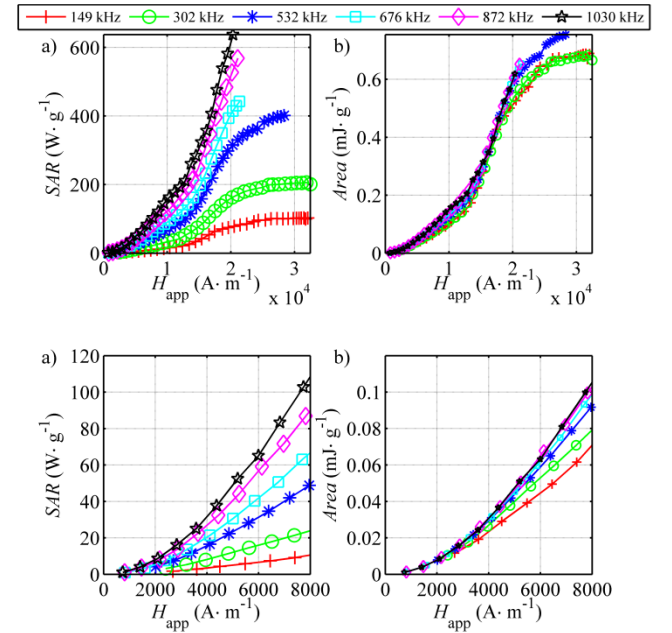


Figure 6. SAR (a) and hysteresis loop area A (b) of oxidized batch 15ff vs. applied intensity H_{app} . As can be appreciated on the zoomed curves (bottom line), the 15ff sample behaves as superparamagnetic at low field (SAR varies as the square of H_{app}). At higher field, it rather shows ferromagnetic behavior with a hysteresis area that first rises above a threshold field intensity and then reaches a plateau.

Whereas an ILP parameter was introduced in literature by dividing the SAR by frequency and by the square of

H_{app} ,¹ the assumption that SAR is a quadratic function holds only at low field amplitude (**Figure 6 a**). Therefore we prefer here to report the ratio of the SAR by frequency only expressed in $J \cdot g^{-1}$, which represents the area A of a hysteresis loop, *i.e.* the thermal losses per one AMF cycle. This method enables comparing the heating properties of the magnetic NPs synthesized in this work to other ones reported in literature, although they were measured under different conditions and setups. As reported by Carrey *et al.*,²⁹ the plot of hysteresis surface area vs. H_{app} expected for ferromagnetic NPs exhibits a sigmoidal shape: it starts from a slow increase as long as the AMF amplitude is lower than the anisotropy field of the material H_{an} , then it varies rapidly (*i.e.* with an exponent larger than two, value expected for superparamagnetic NPs), and finally A tends to a plateau in the high-field limit. This is exactly the profile of the plot of A vs. H_{app} for sample 15ff (**Figure 6 b**), with a threshold anisotropy field $H_{an} \sim 10^4 A \cdot m^{-1}$. The plateau limit of the area per AMF cycle around $0.7 mJ \cdot g^{-1}$ for oxidized 15ff is not exceptional as a maximal value of $1.8 mJ \cdot g^{-1}$ was previously reported for iron oxide NPs obtained after hydrothermal treatment.³⁴ However, sample 15ff illustrates the complex magnetic nanoflower behavior, reflected in the dependence of their hysteresis loss area A with the amplitude H_{app} of the AMF: For the six probed frequencies, the plots of the hysteresis area A vs. H_{app} collapse on a master curve. The field dependence remains quadratic up to a threshold H_{app} ascribed to the anisotropy field H_{an} of the multi-core structure, characteristic of collective dynamics of sintered grains as in a multiple-domain magnet. For applied AMF intensities below H_{an} , nanoflowers exhibit pure superparamagnetic response as seen from the quadratic variation of their SAR vs. H_{app} , each of their magnetic mono-domains being excited individually by the AMF. The other NP samples of lower sizes (below 30 nm) exhibit even superior plateau values of the hysteresis area per cycle vs. H_{app} depending on frequency, from $1.6 mJ \cdot g^{-1}$ for smooth 34ff nanospheres (**Figure S10**) to $2.5 mJ \cdot g^{-1}$ for 35ff nanoflowers (**Figure S12**) or $2 mJ \cdot g^{-1}$ at the lowest frequency of 149 kHz. To our knowledge, these are the highest hysteresis area values published so far for synthetic iron oxide magnetic NPs.

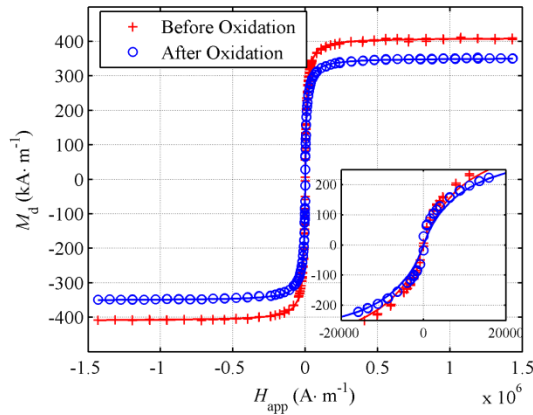


Figure 7. Static magnetization curve of sample 15ff measured by VSM before (red curve) and after oxidation (blue curve).

To get an insight into peculiar structure-property relationship and complex magnetic behavior of nanoflowers, the DC magnetization curves were also measured with a VSM setup for 15ff NPs with or without the oxidation step (**Figure 7**). In both cases, the NPs were dispersed in water acidified with HNO_3 (pH~2.5). The magnetization curve of both samples exhibits null coercive field ($H_c=0$) and zero remanence ($M_r=0$), which corresponds to the superparamagnetic behavior. This evidences good dispersion state of the NPs in water, as a remnant magnetization would have been expected in case of aggregated samples. The saturation magnetization of the un-oxidized sample obtained after synthesis and washings is $350 kA \cdot m^{-1}$, slightly below the value $400 kA \cdot m^{-1}$ of bulk magnetite (Fe_3O_4), as ascribed to spin-canting defects at the NP surface,³⁵ or to partial oxidation already starting during the purification steps, as no particular precautions were taken to prevent it. On the contrary, total oxidation of sample 15ff was favored by heating with iron(III) nitrate, leading to a magnetization at saturation of $300 kA \cdot m^{-1}$, which is the expected value for bulk maghemite ($\gamma-Fe_2O_3$). It was decided to intentionally oxidize every batch produced in order to keep a control over the magnetic phase of the NPs, although at the cost of lowering the magnetic saturation and presumably their heating efficiency for MFH. Other samples reported in this study exhibit similar saturation magnetization (**Figure S4**).

Another information provided by VSM magnetometry can be gathered by fitting the DC magnetization curves by the Langevin function characteristic of superparamagnetism, convolved by a log-normal distribution of diameters to take into account size-dispersity.²¹ The resulting magnetic domain diameters lay below the outer diameter measured on TEM images for nanoflowers: 25.1 ± 12.0 nm for 35ff, 21.9 ± 10.6 nm for 31ff, while it is almost perfectly equal to the TEM diameter (within experimental uncertainty) for 34ff smooth nanospheres: 18.8 ± 6.5 nm.

SQUID magnetometry performed on oxidized and un-oxidized 15ff samples (**Figure S13**) led to ZFC and FC magnetization curves vs. temperature which are both lower for un-oxidized 15ff compared to oxidized 15ff NPs. Such non-classical ZFC-FC curve profile has been already reported for large (18 and 22 nm) Fe_3O_4 NPs synthesized by iron(III) oleate thermal decomposition,³⁶ and was partially explained by the so-called Verwey transition:^{36, 37} The NPs undergo a slight crystallographic distortion from cubic structure (electronically conducting) to inverse spinel (insulating), this change of crystalline structure impacting the magnetic properties of the nanomaterial.

A suitable method to estimate the blocking temperature consists in plotting the derivative of the $M_{FC}-M_{ZFC}$ curve difference with respect to temperature.³⁸ Here it exhibits three maxima for both batches (**Figure S13**): The peak near 90K is ascribed to the Verwey transition of magnetite, yet it is not clear why it appears also on the oxidized sample. The two other peaks correspond to characteristic temperatures, respectively near 200 and 300 K. It is rather uncommon for a sample to exhibit two values of the blocking temperature, defined as the transition from

ferrimagnetic to the superparamagnetic regime. One hypothesis is that $T_{B1} \approx 200\text{K}$ is ascribed to individual magnetic domains of diameter $7.4 \pm 1.4\text{ nm}$ and $T_{B2} \approx 300\text{K}$ to the whole magnetic multi-core structure of outer diameter $36.9 \pm 4.8\text{ nm}$.

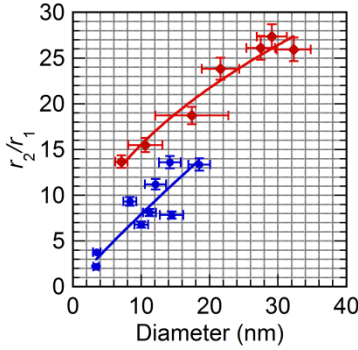


Figure 8. Ratio of transverse to longitudinal relaxivities at 1.41 T/60MHz and 37°C versus average TEM diameters of NPs, for nanosphere (blue) and nanoflower (red) samples. Solid lines are power law fits of exponents respectively 0.92 and 0.48.

In order to assess the efficiency of the different batches synthesized by the polyol route to relax nuclear spins of water protons, their transverse (r_2) and longitudinal (r_1) relaxivities were measured at physiological temperature (37°C) with a 60 MHz relaxometer based on a 1.41 Tesla magnet, i.e. close to the 1.5 Tesla magnetic field of most clinical MRI machines for humans in hospitals (Figure 8). In practice, the longitudinal (T_1) and transverse (T_2) relaxation times of water protons were measured with an inversion-recovery and a CPMG sequence, respectively (see Materials and Methods), for different IONPs at decreasing $[\text{Fe}]$ concentrations starting from 6 mM_{Fe}, and pure water, exhibiting perfect linearity (see Supporting Information).

$$1/T_{i=1 \text{ or } 2} = r_i \times [\text{Fe}] + (1/T_i)_{\text{water}}$$

In the “outer sphere” model of MRI contrast agents introduced by Ayant and Freed for paramagnetic agents, and adapted by Gillis *et al.* to superparamagnetic IONPs,³⁹ the increase relaxation rate $1/T_2$ compared to pure water originates from fluctuating dipolar interactions between nuclear spins of water proton and the electronic magnetic moment of the IONPs. For a limited range of diameters called “motional averaging regime” the superparamagnetic particle can be considered immobile during the echo time of the sequence compared to random trajectories of water molecules diffusing all around the magnetic sphere: In this case, Vuong *et al.* have shown that r_2 follows a scaling law that is quadratic both with the magnetization and with the radius of the “outer sphere”, defined as minimum approach distance between H₂O molecules and the IONP center.⁴⁰ For the IONP batches prepared in this study, the quadratic law is perfectly observed for the smooth sphere NPs (Figure S14), validating the proton diffusive model. This brings further evidence that any organic layer on their surface has been removed by the washing steps, otherwise the water protons could not reach it, and the quadratic law would not hold. In the

case of nanoflowers, the variation of r_2 vs. size appears erratic, presumably because of the rough geometry and high specific area mentioned before (Figure S3): In that case proton relaxivity may arise by a combination of “outer sphere” and “inner sphere” mechanisms, meaning that water molecules can be transiently adsorbed in the porosity of the nanoflowers, thus relaxation dynamics cannot be modelled by a single translational diffusion constant.

In addition, the ratio of relaxivities r_2/r_1 is commonly used to evaluate if NPs are better fit for T_1 (positive) or T_2 (negative) MRI contrast agents applications. With r_2/r_1 ratios larger than 5, most of the IONPs synthesized here are suitable as T_2 weighted MRI contrast agents, like commercial products Resovist®, Feridex®, Clivist® or Clari-scan®.⁴¹ With much smaller r_2/r_1 ratios, UUSPIOs of just a few nm diameters synthesized in pure DEG are rather suitable as T_1 -type, positive contrast agents. Such UUSPIO-based T_1 -type contrast agents are not yet commercially available, as gadolinium-based paramagnetic complexes are preferred, although they are suspected of toxicity.⁴² Gadolinium ions in their un-complexed state are indeed nephrotoxic and neurotoxic, and complications may arise in patients with renal insufficiency: Iron oxides having been proven safe in clinical use, UUSPIOs could have applications in a near future as alternative T_1 contrast agents.

CONCLUSION

This work presented a comprehensive study of IONP synthesis by the forced hydrolysis of iron(II, III) chlorides in DEG polyol either pure or mixed with poly(hydroxy amine) (NMDA). Evidence was brought on the necessity of controlling the amount of water in the reacting medium for a successful synthesis by the polyol pathway and control of the IONP morphology. A large library of samples was obtained, ranging from “ultra-ultra-small” UUSPIOs (~3 nm) obtained by water “hot injection” in DEG at 220°C and fast growth (20 min) to very large ones (up to 37 nm) synthesized through a longer “heating up” protocol, in a DEG/NDMEA 1:1 mixture. Depending on reaction conditions (natural mixing vs. mechanical stirring), either smooth sphere or nanoflower morphologies were obtained. The structural and magnetic properties of these nanoparticles were extensively studied. They all exhibit superparamagnetic behavior characterized by reversible a magnetization curve in static magnetic field, with a strong saturation magnetization, above $3 \cdot 10^5\text{ A}\cdot\text{m}^{-1}$. On the physical side, the specific absorption rate (SAR) was first tested in fixed AMF conditions (755 kHz, 10.2 kA·m⁻¹), then those parameters were varied using a pickup-coil AC magnetometer. Several scaling laws were derived for the SAR and the relaxivity ratio r_2/r_1 , both estimated at 37°C. At given AMF condition, the SAR exhibits quadratic variation with diameter for smooth nanospheres and slower variation (viz. square root) for nanoflowers. Transverse relaxivity r_2 exhibits also quadratic variation with diameter for smooth nanospheres, in line with the “motional averaging regime” of the “outer sphere” model of MRI contrast agents. Then the r_2/r_1 ratio, calculated to show if IONPs are better suited as T_1 or T_2 MRI contrast agents,

varies linearly on diameter for the nanospheres, and with a lower exponent (*viz.* square root) for the nanoflowers.

The AC hysteresis loops measured at varying AMF frequency and intensity brought more information on the magnetic hyperthermia mechanisms: For nanoflowers and large nanospheres, the SAR vs. field intensity curve shows an inflexion point between low and high fields. Below a threshold field they present superparamagnetic behavior, whereas above this field they behave more like ferro-magnets. The threshold field can be associated with an anisotropy field as was done in the two-level Stoner-Wohlfarth model developed by Carrey *et al.* for blocked magnetic moments.²⁹

Applications in magnetic hyperthermia and as MRI contrast agents are envisioned. This versatility of synthesis, morphology and therefore physical properties is achievable playing only on the nature of solvents as well as the amount and way of introducing water in the reaction vessel ("hot injection" vs. "heating up"), in solvent reflux conditions. In brief, robust, gram-scale and easily reproducible synthesis protocols were described to prepare from ultra-ultra-small superparamagnetic cores to very large size magnetic smooth nanospheres and nanoflowers, the latter offering the highest magnetic heating properties reported so far, as found in this study and as described in previous literature on magnetic hyperthermia.

ASSOCIATED CONTENT

Supporting Information. Additional curves (NMR spectra, ζ potential vs. pH, DLS, DC magnetization, ZFC-FC curves, AC hysteresis loops, SAR vs. field, r_1 and r_2 vs. diameter) are accessible in Supporting Information. This material is available free of charge via the Internet at <http://pubs.acs.org>.

AUTHOR INFORMATION

Corresponding Authors

* eneko.garayo@ehu.eus and olivier.sandre@enscbp.fr

Author Contributions

All authors have contributed and given approval to the final version of the manuscript.

Funding Sources

G. H. benefited from a PhD fellowship granted by the Department of Science & Technology of the Univ. Bordeaux (APUB1-ST2014). A. K.'s internship was supported by the US-France-Belgium iREU Site in Translational Chemistry funded by the National Science Foundation (Grant No. 1560390) headed by Pr Randall J. Duran. Basque Government (Grant No. IT-1005-16) and Agence Nationale de la Recherche (Grant ANR-13-BS08-0017 MagnetoChemoBlast) are also acknowledged for financial support. This article is based upon work from COST Action RADIOMAG (TD1402), supported by COST (European Cooperation in Science and Technology).

ACKNOWLEDGMENT

TEM images were taken at the Bordeaux Imaging Center (BIC) of the Univ. Bordeaux with the acknowledged help of Sabrina Lacomme and Etienne Gontier on equipment funded

by France Life Imaging. Authors also want to thank SGiker (UPV/EHU) for the technical and human support as well as the VSM and ZFC-FC measurements.

ABBREVIATIONS

AMF, alternating magnetic field; DEG, diethylene glycol; DLS, dynamic light scattering; *ILP*, intrinsic loss power; IONP, iron oxide nanoparticle; IEP, isoelectric point; MFH, magnetic fluid hyperthermia; NMDEA, *N*-methyl diethanolamine; OD, optical density (or absorbance); SANS, small angle neutron scattering; SAR, specific absorption rate. UUSPIO, ultra-ultra small superparamagnetic iron oxide.

REFERENCES

1. Hervault, A.; Thanh, N. T. K., Magnetic nanoparticle-based therapeutic agents for thermo-chemotherapy treatment of cancer. *Nanoscale* 2014, 6, (20), 11553-11573.
2. Périgo, E. A.; Hemery, G.; Sandre, O.; Ortega, D.; Garaio, E.; Plazaola, F.; Teran, F. J., Fundamentals and advances in magnetic hyperthermia. *Applied Physics Reviews* 2015, 2, (4), 041302.
3. Massart, R., Preparation of aqueous magnetic liquids in alkaline and acidic media. *IEEE Transactions on Magnetics* 1981, 17, (2), 1247-1248.
4. Caruntu, D.; Caruntu, G.; Chen, Y.; O'Connor, C. J.; Goloverda, G.; Kolesnichenko, V. L., Synthesis of Variable-Sized Nanocrystals of Fe₃O₄ with High Surface Reactivity. *Chemistry of Materials* 2004, 16, (25), 5527-5534.
5. Hyeon, T.; Lee, S. S.; Park, J.; Chung, Y.; Na, H. B., Synthesis of Highly Crystalline and Monodisperse Maghemite Nanocrystallites without a Size-Selection Process. *J. Am. Chem. Soc.* 2001, 123, (51), 12798-12801.
6. Horner, O.; Neveu, S.; Montredon, S. d.; Siaugue, J.-M.; Cabuil, V., Hydrothermal synthesis of large maghemite nanoparticles: influence of the pH on the particle size. *J. Nanopart. Res.* 2009, 11, (5), 1247-1250.
7. Shubitidze, F.; Kekalo, K.; Stigliano, R.; Baker, I., Magnetic nanoparticles with high specific absorption rate of electromagnetic energy at low field strength for hyperthermia therapy. *Journal of Applied Physics* 2015, 117, (9), 094302.
8. Blanco-Andujar, C.; Ortega, D.; Southern, P.; Pankhurst, Q. A.; Thanh, N. T. K., High performance multi-core iron oxide nanoparticles for magnetic hyperthermia: microwave synthesis, and the role of core-to-core interactions. *Nanoscale* 2015, 7, (5), 1768-1775.
9. Lartigue, L.; Hugounenq, P.; Alloyeau, D.; Clarke, S. P.; Lévy, M.; Bacri, J.-C.; Bazzi, R.; Brougham, D. F.; Wilhelm, C.; Gazeau, F., Cooperative Organization in Iron Oxide Multi-Core Nanoparticles Potentiates Their Efficiency as Heating Mediators and MRI Contrast Agents. *ACS Nano* 2012, 6, (12), 10935-10949.
10. Kostopoulou, A.; Brintakis, K.; Vasilakaki, M.; Trohidou, K. N.; Douvalis, A. P.; Lascialfari, A.; Manna, L.; Lappas, A., Assembly-mediated interplay of dipolar interactions and surface spin disorder in colloidal maghemite nanoclusters. *Nanoscale* 2014, 6, (7), 3764-3776.
11. Caruntu, D.; Remond, Y.; Chou, N. H.; Jun, M.-J.; Caruntu, G.; He, J.; Goloverda, G.; O'Connor, C.; Kolesnichenko, V., Reactivity of 3d Transition Metal Cations in Diethylene Glycol Solutions. Synthesis of Transition Metal Ferrites with the Structure of Discrete Nanoparticles Complexed with Long-Chain Carboxylate Anions. *Inorganic Chemistry* 2002, 41, (23), 6137-6146.
12. Cheng, C.; Xua, F.; Gu, H., Facile synthesis and morphology evolution of magnetic iron oxide nanoparticles in different polyol processes. *New J. Chem.* 2011, 35, 1072-1079.
13. Hachani, R.; Lowdell, M.; Birchall, M.; Hervault, A.; Mertz, D.; Begin-Colin, S.; Thanh, N. T. K., Polyol synthesis, functional-

sation, and biocompatibility studies of superparamagnetic iron oxide nanoparticles as potential MRI contrast agents. *Nanoscale* 2016, 8, (6), 3278–3287.

14. Hugounenq, P.; Levy, M.; Alloyeau, D.; Lartigue, L.; Dubois, E.; Cabuil, V.; Ricolleau, C.; Roux, S.; Wilhelm, C.; Gazeau, F.; Bazzi, R., Iron Oxide Monocrystalline Nanoflowers for Highly Efficient Magnetic Hyperthermia. *J. Phys. Chem. C* 2012, 116, (29), 15702–15712.

15. Forge, D.; Roch, A.; Laurent, S.; Tellez, H.; Gossuin, Y.; Renaux, F.; Vander Elst, L.; Muller, R. N., Optimization of the Synthesis of Superparamagnetic Contrast Agents by the Design of Experiments Method. *The Journal of Physical Chemistry C* 2008, 112, (49), 19178–19185.

16. Sakellari, D.; Brintakis, K.; Kostopoulou, A.; Myrovali, E.; Simeonidis, K.; Lappas, A.; Angelakeris, M., Ferrimagnetic nanocrystal assemblies as versatile magnetic particle hyperthermia mediators. *Materials Science and Engineering: C* 2016, 58, 187–193.

17. Tourinho, F. A.; Franck, R.; Massart, R., Aqueous ferrofluids based on manganese and cobalt ferrites. *Journal of Materials Science* 1990, 25, (7), 3249–3254.

18. Koppel, D. E., Analysis of Macromolecular Polydispersity in Intensity Correlation Spectroscopy: The Method of Cumulants. *The Journal of Chemical Physics* 1972, 57, (11), 4814–4820.

19. Henoumont, C.; Laurent, S.; Vander Elst, L., How to perform accurate and reliable measurements of longitudinal and transverse relaxation times of MRI contrast media in aqueous solutions. *Contrast Media & Molecular Imaging* 2009, 4, (6), 312–321.

20. Hemery, G.; Garanger, E.; Lecommandoux, S.; Wong, A. D.; Gillies, E. R.; Pedrono, B.; Bayle, T.; Jacob, D.; Sandre, O., Thermosensitive polymer-grafted iron oxide nanoparticles studied by in situ dynamic light backscattering under magnetic hyperthermia. *Journal of Physics D: Applied Physics* 2015, 48, (49), 494001.

21. Garaio, E.; Sandre, O.; Collantes, J.-M.; Garcia, J. A.; Mornet, S.; Plazaola, F., Specific absorption rate dependence on temperature in magnetic field hyperthermia measured by dynamic hysteresis losses (ac magnetometry). *Nanotechnology* 2015, 26, (1), 015704.

22. Tromsdorf, U. I.; Bruns, O. T.; Salmen, S. C.; Beisiegel, U.; Weller, H., A Highly Effective, Nontoxic T₁ MR Contrast Agent Based on Ultrasmall PEGylated Iron Oxide Nanoparticles. *Nano Letters* 2009, 9, (12), 4434–4440.

23. Ninjbadgar, T.; Brougham, D. F., Epoxy Ring Opening Phase Transfer as a General Route to Water Dispersible Superparamagnetic Fe₃O₄ Nanoparticles and Their Application as Positive MRI Contrast Agents. *Advanced Functional Materials* 2011, 21, (24), 4769–4775.

24. Borase, T.; Ninjbadgar, T.; Kapetanakis, A.; Roche, S.; O'Connor, R.; Kerskens, C.; Heise, A.; Brougham, D. F., Stable Aqueous Dispersions of Glycopeptide-Grafted Selectably Functionalized Magnetic Nanoparticles. *Angewandte Chemie International Edition* 2013, 52, (11), 3164–3167.

25. Hannecart, A.; Stanicki, D.; Vander Elst, L.; Muller, R. N.; Lecommandoux, S.; Thevenot, J.; Bonduelle, C.; Trotier, A.; Massot, P.; Miraux, S.; Sandre, O.; Laurent, S., Nanothermometers with thermo-sensitive polymer grafted USPIOs behaving as positive contrast agents in low-field MRI. *Nanoscale* 2015, 7, (8), 3754–3767.

26. Sanz, B.; Calatayud, M. P.; De Biasi, E.; Lima, E., Jr.; Mansilla, M. V.; Zysler, R. D.; Ibarra, M. R.; Goya, G. F., In Silico before In Vivo: how to Predict the Heating Efficiency of Magnetic Nanoparticles within the Intracellular Space. *Sci Rep.* 2016, 6, 38733.

27. Jacob, N.; Schinteie, G.; Palade, P.; Ticos, C. M.; Kuncser, V., Stepped heating procedure for experimental SAR evaluation of ferrofluids. *The European Physical Journal E* 2015, 38, (6), 57.

28. Kallumadil, M.; Tada, M.; Nakagawa, T.; Abe, M.; Southern, P.; Pankhurst, Q. A., Suitability of commercial colloids for magnetic hyperthermia. *Journal of Magnetism and Magnetic Materials* 2009, 321, (10), 1509–1513.

29. Carrey, J.; Mehdaoui, B.; Respaud, M., Simple models for dynamic hysteresis loop calculations of magnetic single-domain nanoparticles: Application to magnetic hyperthermia optimization. *Journal of Applied Physics* 2011, 109, (8), 083921.

30. Garaio, E.; Collantes, J. M.; Garcia, J. A.; Plazaola, F.; Mornet, S.; Couillaud, F.; Sandre, O., A wide-frequency range AC magnetometer to measure the specific absorption rate in nanoparticles for magnetic hyperthermia. *Journal of Magnetism and Magnetic Materials* 2014, 368, 432–437.

31. Lacroix, L.-M.; Malaki, R. B.; Carrey, J.; Lachaize, S.; Respaud, M.; Goya, G. F.; Chaudret, B., Magnetic hyperthermia in single-domain monodisperse FeCo nanoparticles: Evidences for Stoner–Wohlfarth behavior and large losses. *Journal of Applied Physics* 2009, 105, (2), 023911.

32. Mehdaoui, B.; Meffre, A.; Carrey, J.; Lachaize, S.; Lacroix, L.-M.; Gougeon, M.; Chaudret, B.; Respaud, M., Optimal Size of Nanoparticles for Magnetic Hyperthermia: A Combined Theoretical and Experimental Study. *Advanced Functional Materials* 2011, 21, (23), 4573–4581.

33. Hergt, R.; Dutz, S., Magnetic particle hyperthermia—biophysical limitations of a visionary tumour therapy. *Journal of Magnetism and Magnetic Materials* 2007, 311, (1), 187–192.

34. Marciello, M.; Connord, V.; Veintemillas-Verdaguer, S.; Verges, M. A.; Carrey, J.; Respaud, M.; Serna, C. J.; Morales, M. P., Large scale production of biocompatible magnetite nanocrystals with high saturation magnetization values through green aqueous synthesis. *Journal of Materials Chemistry B* 2013, 1, (43), 5995–6004.

35. Baaziz, W.; Pichon, B. P.; Fleutot, S.; Liu, Y.; Lefevre, C.; Greneche, J.-M.; Toumi, M.; Mhiri, T.; Begin-Colin, S., Magnetic Iron Oxide Nanoparticles: Reproducible Tuning of the Size and Nanosized-Dependent Composition, Defects, and Spin Canting. *The Journal of Physical Chemistry C* 2014, 118, (7), 3795–3810.

36. Salas, G.; Casado, C.; Teran, F. J.; Miranda, R.; Serna, C. J.; Morales, M. P., Controlled synthesis of uniform magnetite nanocrystals with high-quality properties for biomedical applications. *Journal of Materials Chemistry* 2012, 22, (39), 21065–21075.

37. Goya, G. F.; Berquó, T. S.; Fonseca, F. C.; Morales, M. P., Static and dynamic magnetic properties of spherical magnetite nanoparticles. *Journal of Applied Physics* 2003, 94, (5), 3520–3528.

38. Bruvera, I. J.; Mendoza Zélis, P.; Pilar Calatayud, M.; Goya, G. F.; Sánchez, F. H., Determination of the blocking temperature of magnetic nanoparticles: The good, the bad, and the ugly. *Journal of Applied Physics* 2015, 118, (18), 184304.

39. Gillis, P.; Roch, A.; Brooks, R. A., Corrected Equations for Susceptibility-Induced T₂-Shortening. *Journal of Magnetic Resonance* 1999, 137, (2), 402–407.

40. Vuong, Q. L.; Berret, J.-F.; Fresnais, J.; Gossuin, Y.; Sandre, O., A Universal Scaling Law to Predict the Efficiency of Magnetic Nanoparticles as MRI T₂-Contrast Agents. *Advanced Healthcare Materials* 2012, 1, (4), 502–512.

41. Wang, Y.-X. J., Superparamagnetic iron oxide based MRI contrast agents: Current status of clinical application. *Quantitative Imaging in Medicine and Surgery* 2011, 1, (1), 35–40.

42. Thomsen, H. S.; Morcos, S. K.; Dawson, P., Is there a causal relation between the administration of gadolinium based contrast media and the development of nephrogenic systemic fibrosis (NSF)? *Clinical Radiology* 2006, 61, (11), 905–906.

Tuning sizes, morphologies, and magnetic properties of mono- vs. multi-core iron oxide nanoparticles through control of added water in the polyol synthesis

Gauvin Hemery^a, Anthony C. Keyes Jr.^a, Eneko Garaio^{b*}, Irati Rodrigo^{b,c}, Jose Angel Garcia^{c,d}, Fernando Plazaola^b, Elisabeth Garanger^a, Olivier Sandre^{a*}

^a LCPO, CNRS UMR 5629/ Univ. Bordeaux/ Bordeaux-INP, ENSCBP 16 avenue Pey Berland, 33607 Pessac, France

^b Elektrizitatea eta Elektronika Saila, UPV/EHU, 48940 Leioa, Spain

^c BCMaterials, Parque Tecnológico de Bizkaia, Ed. 50, 48160 Derio, Spain

^d Fisika Aplikatua II Saila, UPV/EHU, 48940 Leioa, Spain

KEYWORDS: Polyol synthesis, iron oxide, nanoparticles, magnetic hyperthermia, MRI contrast agent, nanoflowers

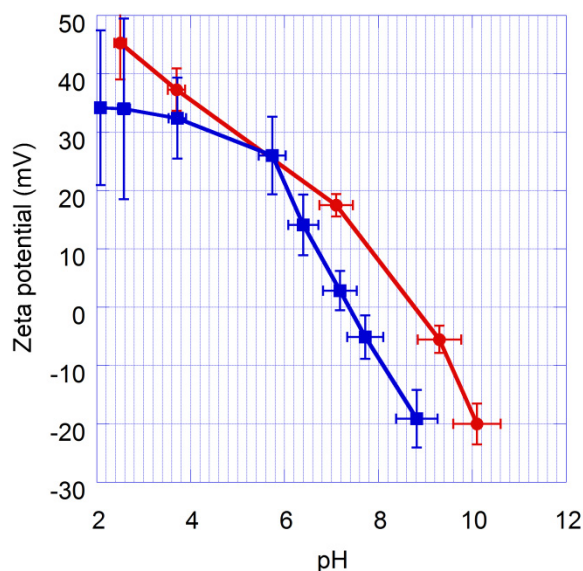


Figure S1. Zeta potential measurement of IONPs which surfaces are partially cleaned after the polyol synthesis (red circles), with an isoelectric point (IEP) estimated to be at around pH=9, evidencing the presence of amine moieties of NMEDEA of the solvent molecules chelated on the IONPs. IONPs fully cleaned (blue squares), with an IEP estimated to be around pH=7, which is consistent with values previously reported for bare iron oxide surface.

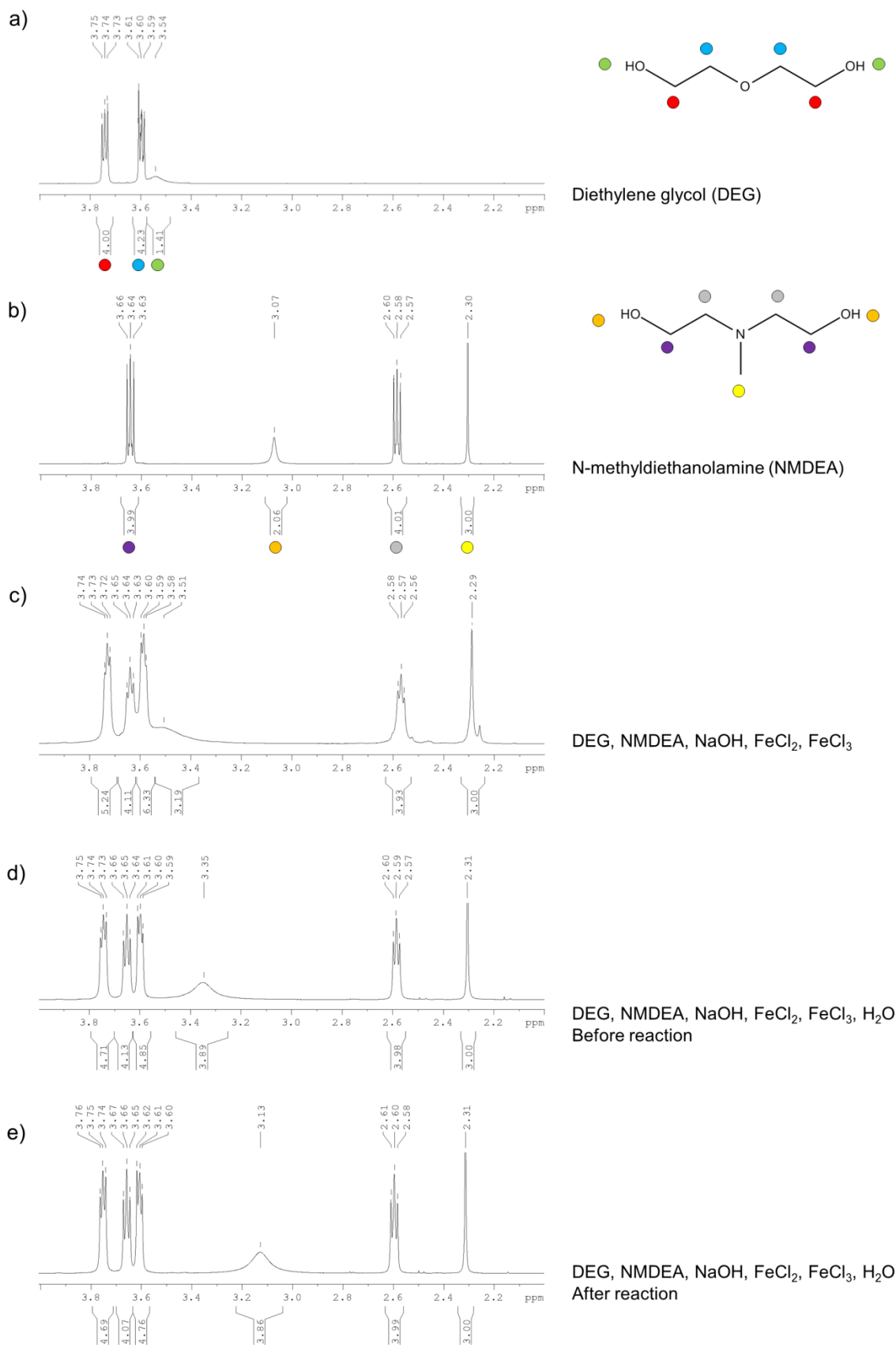


Figure S2. NMR analyses of DEG (a), NMDEA (b) and of the medium of synthesis before addition of water (c), after addition of water (d) and after reaction (e). Addition of water shifts the peak corresponding to hydroxyls, which is further shifted after reaction, possibly because of a variation of pH. The solvents do not undergo degradation during the reaction.

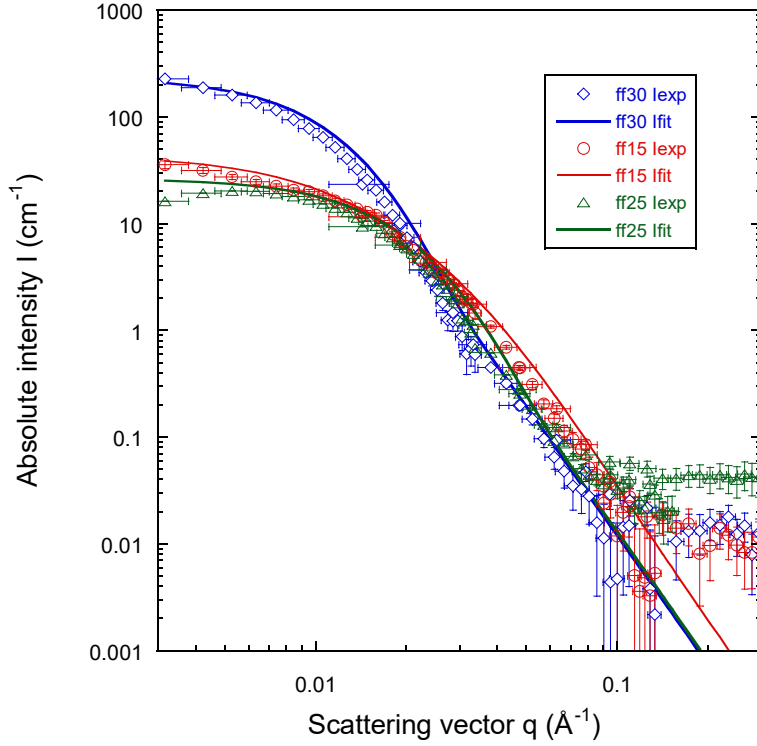


Figure S3. Small angle neutron scattering curves of samples 30ff (nanoflowers), 15ff (nanoflowers) and 25ff (smooth spheres). Solid lines represent fits with polydisperse sphere form factor corresponding to following values of the intensity-average radius determined by SANS, to compare with the gyration radius by SANS and the radius obtained by TEM analysis. The specific area was estimated by the Porod law (given the concentration and the theoretical neutron scattering contrast of iron oxide in water).

$$30\text{ff: } R_G=18.9 \text{ nm}, R_{\text{SANS}}=18.1 \pm 3.9 \text{ nm}, R_{\text{TEM}}=23.5 \pm 4.2 \text{ nm}, A_{\text{spe}}=31.3 \text{ m}^2 \cdot \text{g}^{-1}$$

$$15\text{ff: } R_G=19.0 \text{ nm}, R_{\text{SANS}}=10.6 \pm 1.8 \text{ nm}, R_{\text{TEM}}=17.5 \pm 2.4 \text{ nm}, A_{\text{spe}}=82.4 \text{ m}^2 \cdot \text{g}^{-1}$$

$$25\text{ff: } R_G=10.5 \text{ nm}, R_{\text{SANS}}=10.4 \pm 2.3 \text{ nm}, R_{\text{TEM}}=7.1 \pm 1.6 \text{ nm}, A_{\text{spe}}=71.2 \text{ m}^2 \cdot \text{g}^{-1}$$

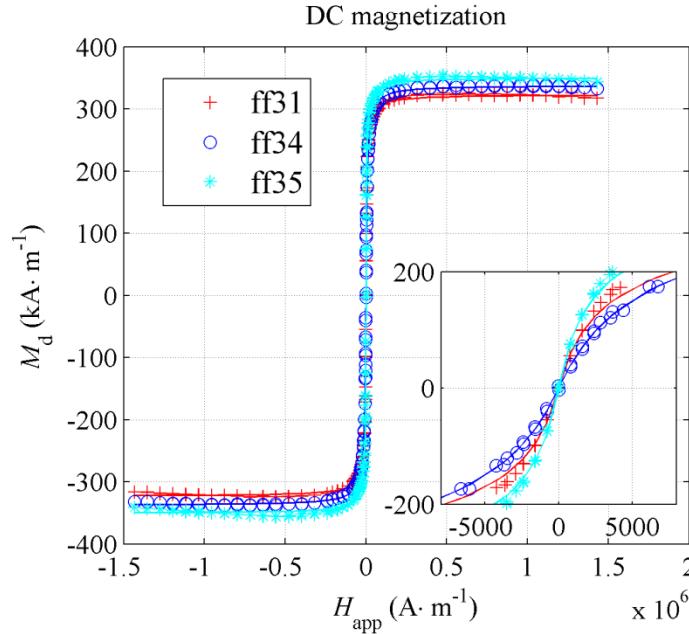


Figure S4. DC magnetization of samples 31ff, 34ff and 35ff measured by VSM. As the inset shows, they follow a superparamagnetic behavior. The signal was normalized by volume fraction calculated from the iron oxide concentration (assuming a mass density of $5 \text{ g} \cdot \text{cm}^3$) in order to derive the specific magnetization per domain, denominated M_d .

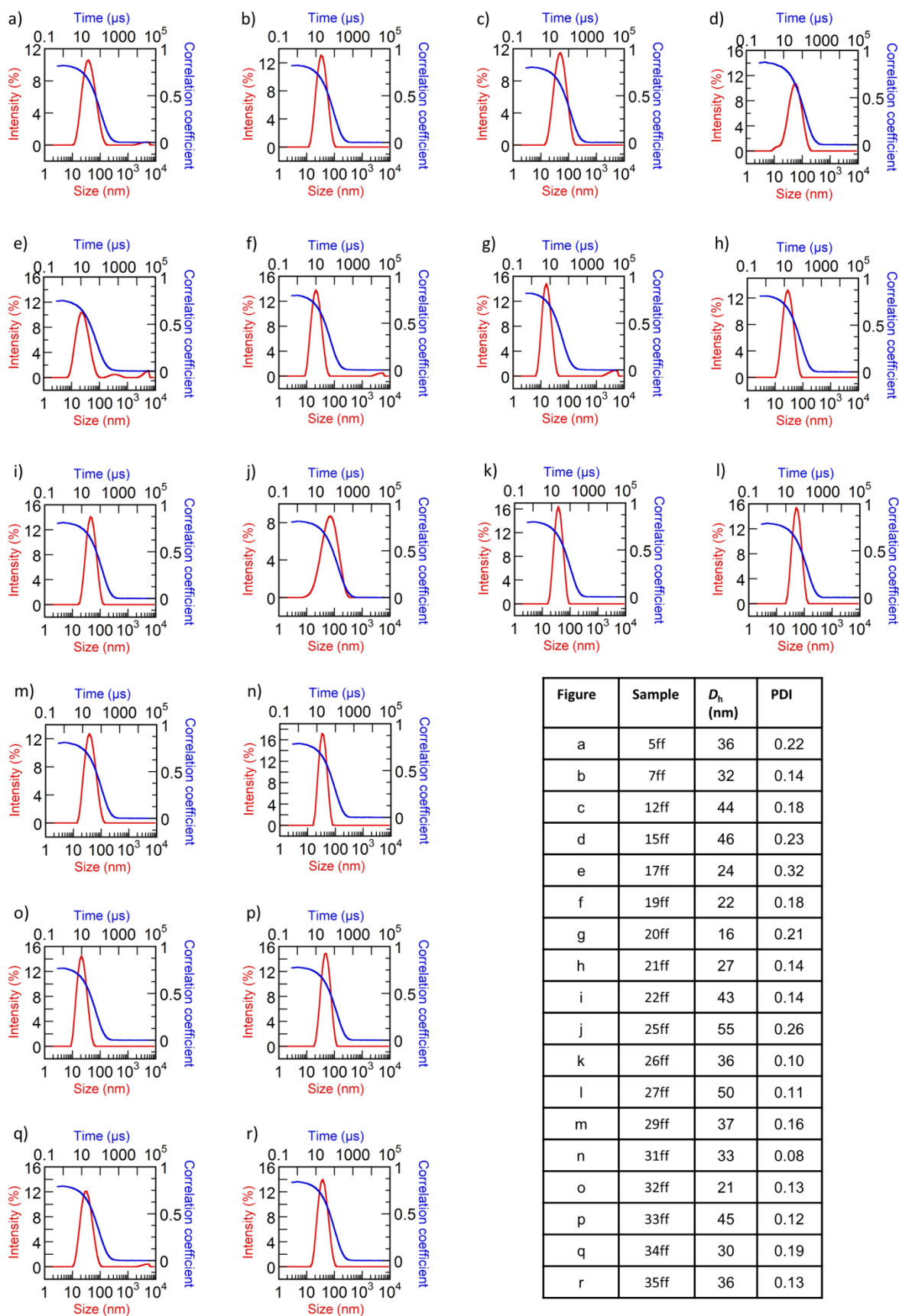


Figure S5. DLS correlograms and intensity-averaged distribution of diameters. The 2nd order cumulant fit leads to the Z-average hydrodynamic diameter (D_h) and polydispersity index (PDI).

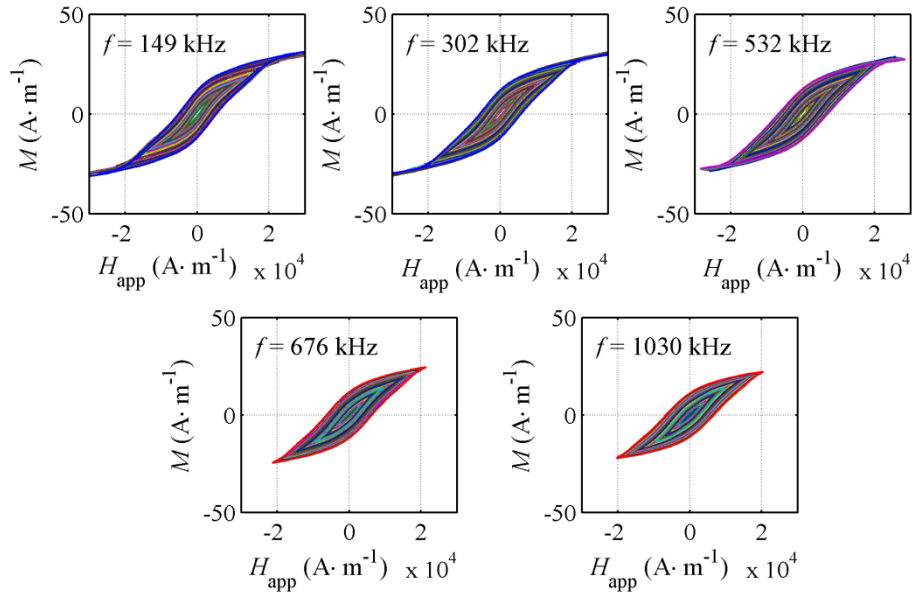


Figure S6. AC hysteresis cycles of oxidized 15ff sample (nanoflowers of grain size 7.4 ± 1.4 nm and outer diameter 36.9 ± 4.8 nm) at different AMF amplitudes H_{app} and frequencies (f). The superimposed black line is the DC magnetization measured by VSM.

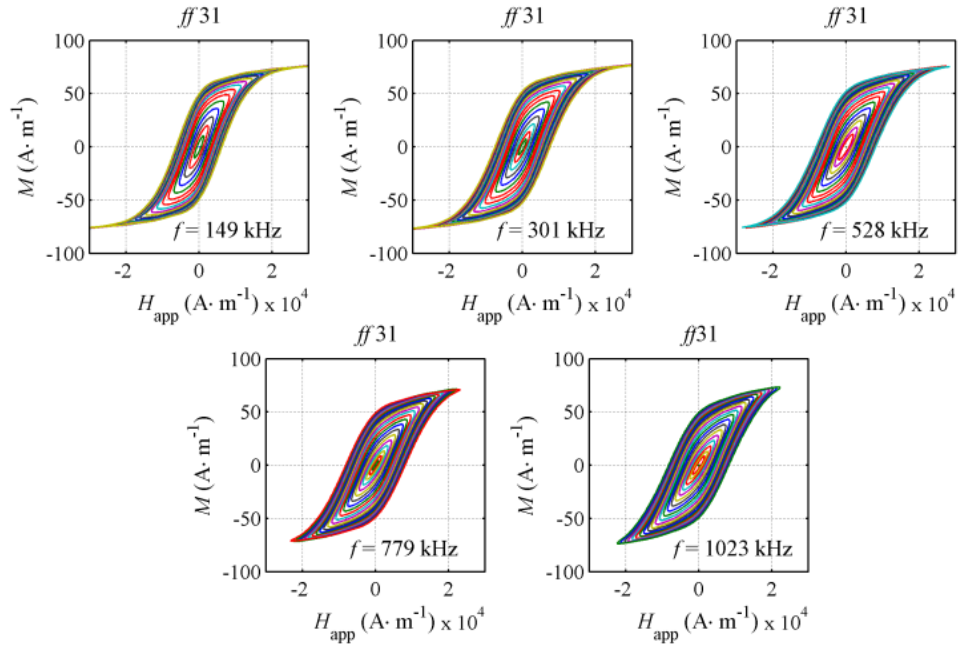


Figure S7. AC hysteresis cycles of 31ff sample (nanoflowers of 27.5 ± 4.2 nm outer diameter) at different field amplitudes H_{app} and frequencies (f).

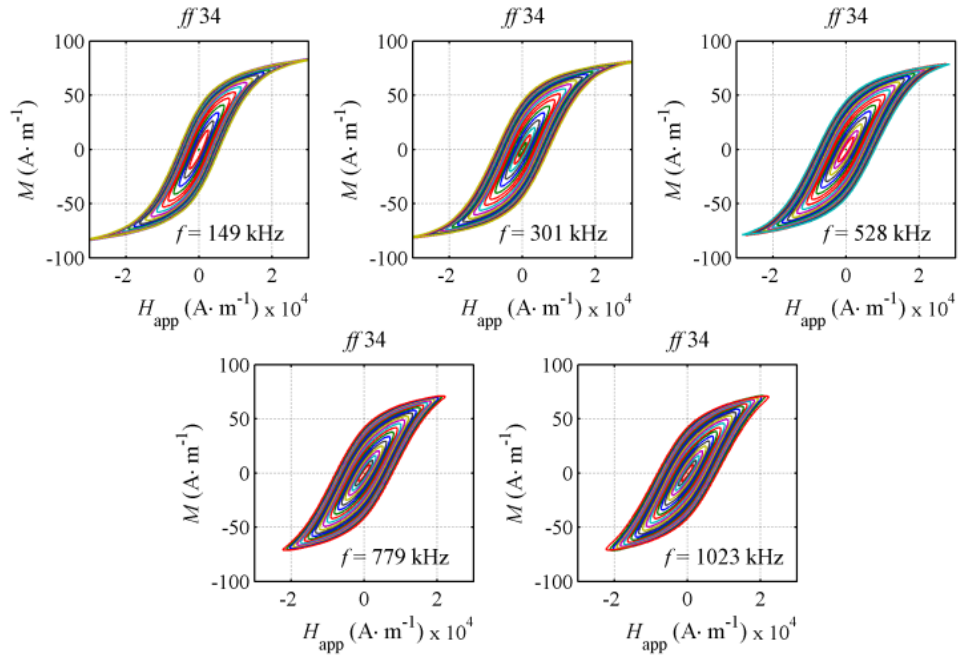


Figure S8. AC hysteresis cycles of 34ff sample (smooth nanospheres of 18.5 ± 3.2 nm diameter) at different field amplitudes H_{app} and frequencies (f).

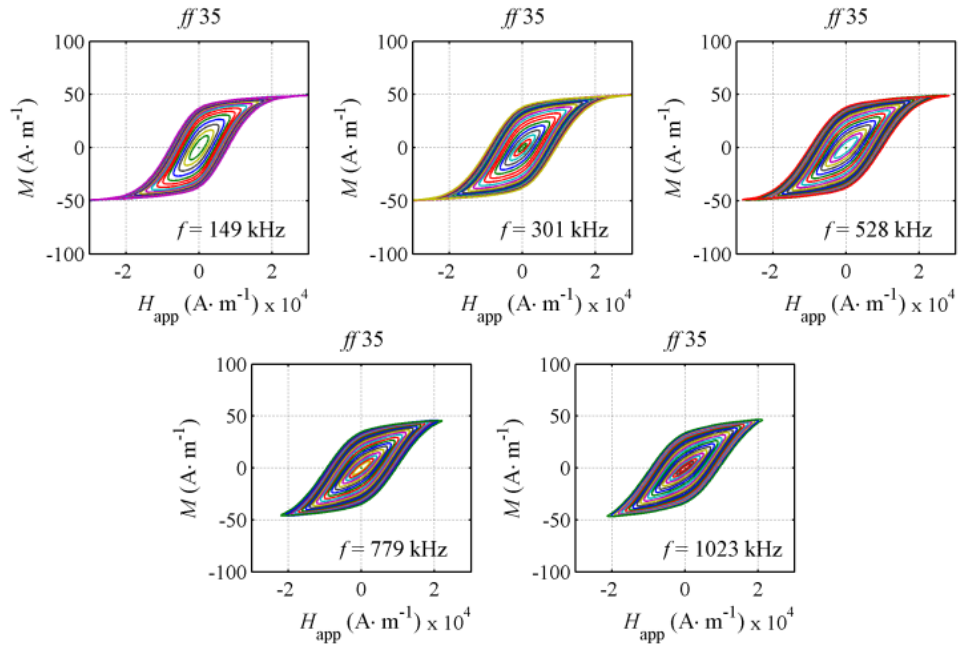


Figure S9. AC hysteresis cycles of 35ff sample (nanoflowers of 29.1 ± 4.4 nm outer diameter) at different field amplitudes H_{app} and frequencies (f).

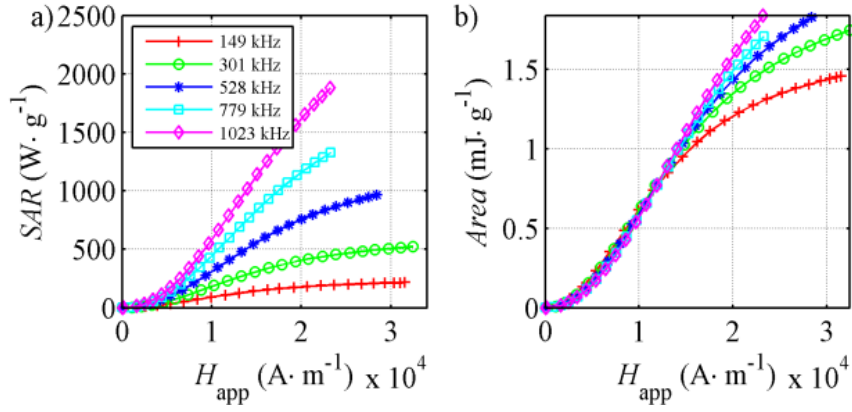


Figure S10. SAR (a) and hysteresis area (b) of sample 31ff (nanoflowers of 27.5 ± 4.2 nm outer diameter) *versus* applied magnetic field amplitude (H_{app}).

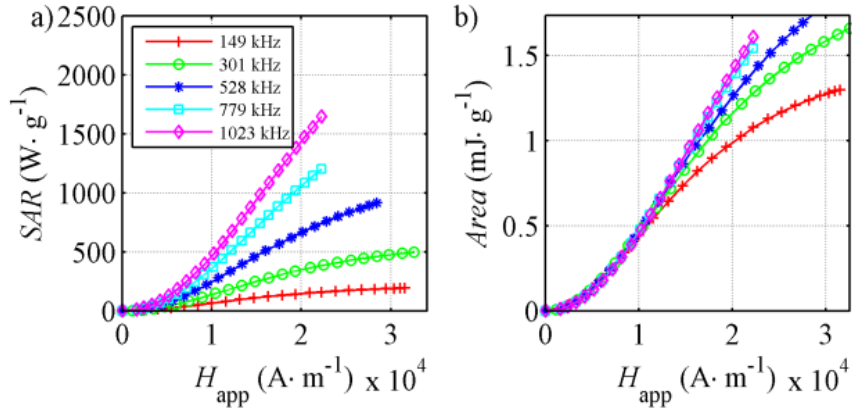


Figure S11. SAR (a) and hysteresis area (b) of sample 34ff (smooth nanospheres of 18.5 ± 3.2 nm diameter) *versus* applied magnetic field amplitude (H_{app}).

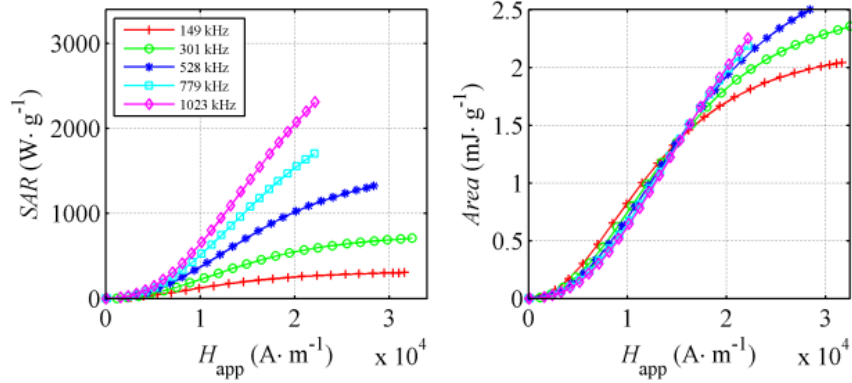


Figure S12. SAR (a) and hysteresis area (b) of sample 35ff (nanoflowers of 29.1 ± 4.4 nm outer diameter) *versus* applied magnetic field amplitude (H_{app}).

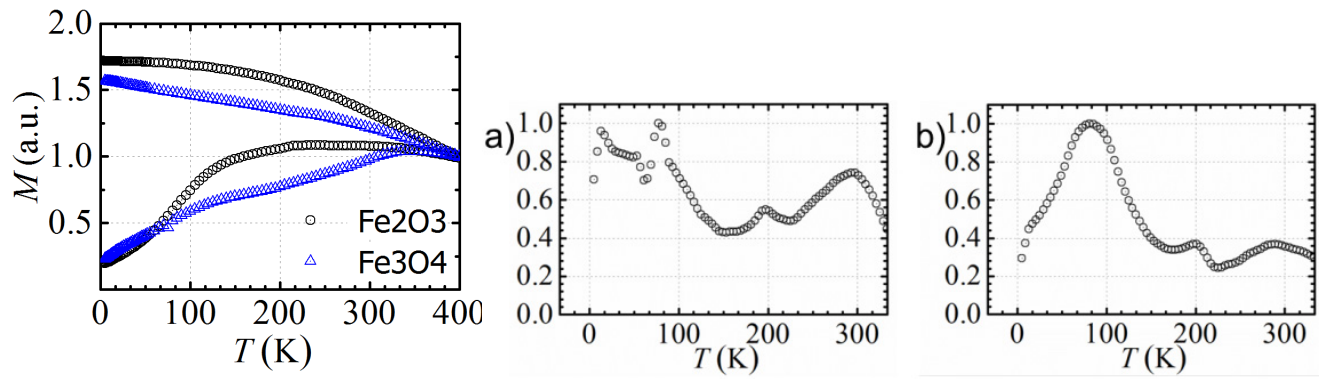


Figure S13. ZFC-FC measurement by SQUID magnetometry and derivative $d(M_{\text{FC}} - M_{\text{ZFC}})/dT$ of the FC-ZFC curve difference for un-oxidized Fe_3O_4 (a) and oxidized $\gamma\text{-Fe}_2\text{O}_3$ (b) 15ff nanoflowers. The peak near 90K is ascribed to the Verwey transition.

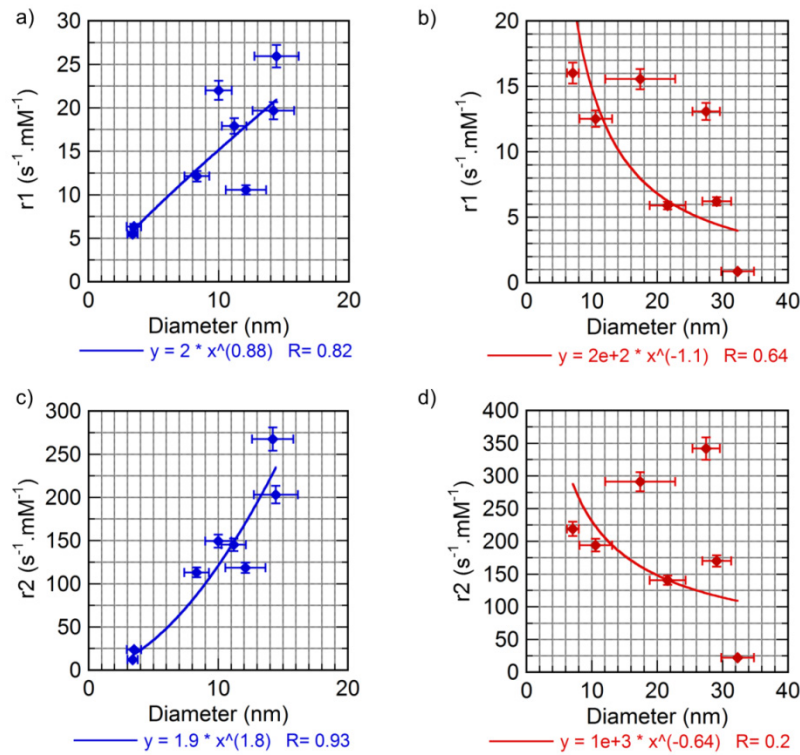


Figure S14. Longitudinal relaxivity of smooth spheres (a) and nanoflowers (b). Transverse relaxivity of smooth spheres (c) and nanoflowers (d). All measurements were performed at 37°C in a 1.41 Tesla / 60 MHz Bruker mq60 relaxometer.